PNAS RESEARCH ARTICLE | EARTH, ATMOSPHERIC, AND PLANETARY SCIENCES

In situ evidence of self-accelerating turbidity currents

Hongbo Ma[a,b,1,2], Gefei Deng[a,1], Xingyu Chen[a], Yuanjian Wang[c,2], Brandon McElroy[d], Jeffrey Nittrouer[e], Yu Zhang[a], Toshiki Iwasaki[f], Matthieu Cartigny[g], and Xudong Fu[a,2]

Affiliations are included on p. 8.

Edited by Michael Manga, University of California, Berkeley, CA; received January 14, 2026; accepted April 23, 2026

Self-accelerating turbidity currents (SATCs) are hypothesized to be the primary mechanism for transporting vast amounts of sediment to the deep ocean. However, theoretical predictions of SATCs have preceded field observations by decades, leaving a critical gap in our understanding of this long-distance delivery process. Here, we present results from a four-year field survey of turbidity currents and bathymetric evolution in the Xiaolangdi Reservoir on the Yellow River (China), the world's most sediment-laden river. We provide definitive in situ evidence of SATCs, characterized by synchronous down-channel increases in sediment mass and current momentum, alongside massive channel incision at the event scale. Notably, these SATCs occur in a low-gradient lacustrine setting, challenging the prevailing hypothesis that such phenomena are restricted to steep submarine channels or high velocity conditions. We identify a dimensionless threshold, incorporating current velocity, channel slope, and sediment settling velocity, that governs SATC formation across sublacustrine and marine environments. This threshold provides a robust framework for predicting SATC occurrence and informs engineering strategies to sustain reservoir capacity and restore sediment connectivity in dammed river systems.

turbidity currents | self-accelerating | in situ | erosion | reservoir

Significance

Self-accelerating turbidity currents are powerful, erosive gravity underflows that sever intercontinental telecommunication cables and reshape subaqueous landscapes. Despite their significance, direct field observations of their growth and intensification have remained elusive. Using the Xiaolangdi Reservoir as a natural laboratory, this study provides in situ evidence that erosive turbidity currents develop even in low-slope environments, contradicting the belief that steep gradients or high velocities are prerequisites for acceleration. The identified universal threshold offers a predictive tool for submarine geohazard assessment and reservoir sedimentation management. These findings provide a physical basis for utilizing these currents to bypass and erode reservoir sediment, restoring sediment connectivity and mitigating the global reservoir sedimentation crisis, which currently reduces global storage capacity by approximately 1% annually.

Turbidity currents constitute a major long-distance sediment delivery mechanism in submarine and lacustrine environments (1). These stratified flows enable the long-distance transport of passive and active tracers, such as microplastics and mineral-associated organic carbon, in the marine environment (2–6). They thus provide the primary link between their terrestrial sources and the deep-sea sink (7–9). Their presence on subaqueous deltas and shelves is widely considered a major constructive mechanism (10, 11), and estimating their load is therefore essential to reconstruct sedimentary histories (12, 13). Turbidity currents can be very powerful, occasionally breaking intercontinental telecommunication cables (9, 14–16), while hydraulic engineers use this phenomenon to sluice sediment from man-made reservoirs through dams to mitigate reservoir sedimentation (17). In both settings, it is natural to ask how powerful turbidity currents are formed. It has long been theorized that turbidity currents can self-accelerate (18–20), where acceleration increases sediment entrainment, entrained sediment adds submerged weight (gravity), and the added gravity (force or energy) further accelerates the current, creating a positive feedback loop. Self-acceleration (also termed ignition) is widely considered to be one of the main mechanisms by which turbidity currents can grow powerful along the way and thus propagate over long distances, until reaching autosuspension (equilibrium) or dying out in unconfined, low-slope channels (16, 21–23). Therefore, it is widely hypothesized that, if they propagate over long distances, turbidity currents must experience self-acceleration, at least in the early stage of development (9, 21).

The mechanism underlying the self-acceleration was first explicitly theorized by Bagnold (24) and Pantin (20), with an energy-balance theory proposed by Knapp (25) and Vlugter (26), and then further developed by Parker (18, 19, 27) from the 1930s to the 1980s (28). However, due to the difficulty at the time of directly measuring such currents (as they commonly occur in deep water), the first verification of the self-acceleration mechanism was achieved decades later in laboratory experiments (29, 30), which set a rigorous standard to identify self-accelerating turbidity currents (SATCs) (30): $D(HC)/Dt > 0$ and $D(HU)/Dt > 0$, where $D\cdot/Dt = \partial\cdot/\partial t + \partial(\cdot U)/\partial x$ is the material derivative, C is the turbidity-current layer-averaged sediment volumetric concentration, H is the layer thickness, and U is the layer-averaged velocity. Hence, $D(HC)/Dt$ is the total sediment volume change in the current as it propagates, and $D(HU)/Dt$ is the total momentum change in the current as it propagates. Both need to be positive, meaning that 1) the sediment volume in the current increases as it propagates and 2) its momentum concurrently increases (accelerates), to confirm that the current is self-accelerating.

The authors declare no competing interest.

This article is a PNAS Direct Submission.

Copyright © 2026 the Author(s). Published by PNAS. This article is distributed under Creative Commons Attribution-NonCommercial-NoDerivatives License 4.0 (CC BY-NC-ND).

[1]H.M. and G.D. contributed equally to this work.

[2]To whom correspondence may be addressed. Email: hongboma@illinois.edu, wangyuanjian_yrcc@aliyun.com, or xdfu@tsinghua.edu.cn.

This article contains supporting information online at https://www.pnas.org/lookup/suppl/doi:10.1073/pnas.2601534123/-/DCSupplemental.

Published May 26, 2026.

Downloaded from https://www.pnas.org by UNIVERSITY OF ILLINOIS URBANA CHAMPAIGN; BIOLOGY LIB E on May 26, 2026 from IP address 130.126.255.117.

However, despite success in small-scale setups, field observations of accelerating turbidity currents have been rare, with only a few cases primarily in submarine settings (9, 21, 22, 31–33). Moreover, since direct sampling of water–sediment mixtures is very difficult in submarine settings (1, 34), measurements of sediment concentration changes downflow are absent [i.e., $D(HC)/Dt$ unknown], making it impossible to confirm that the observed acceleration was caused by sediment entrainment. Direct measurements of sediment concentrations were proposed as one of the goals of future submarine-current surveys (1, 35). Furthermore, both flume and submarine settings have steep channels (9, 21, 29, 30, 36, 37) with slopes ranging from 0.3 to 100%, so it is uncertain whether self-acceleration could occur in a low-slope setup, like lacustrine, abyssal plains, or reservoir environments. More specifically, it has been previously hypothesized that self-acceleration would not occur in low-slope settings (38) because neither Froude-supercritical (30, 39) nor high velocity (9) conditions can be achieved in such settings (38). Here, to address these challenges, we conducted field surveys of turbidity currents at the Xiaolangdi Reservoir (Fig. 1*A*), located on the world's most dense sediment-laden river, the Yellow River, China (40), in 2018–2020 and 2023 (but with the period 2021–2022 absent due to the COVID pandemic). Located at the exit of the water basin, Xiaolangdi Dam is able to retain nearly 100% of the sediment yielded from the rapidly eroding Loess Plateau in its reservoir (41, 42). During the flood season, sediment-laden floods with volumetric concentrations ranging from 0.1 to 30% originating from the Loess Plateau, can easily generate turbidity currents in the reservoir (43–45). The last reservoir (Sanmenxia), constructed in a similar location, filled with sediment, two years after entering service, due to the high sediment yield from the Loess Plateau (46, 47). With this in mind, Xiaolangdi Dam was designed with sediment-sluicing gates near the bottom to vent turbidity currents in the reservoir, significantly mitigating reservoir sedimentation (46, 47). To date, Xiaolangdi Dam has been in service for more than two and a half decades and continues to serve for flood control, freshwater supply, and power generation.

Compared to the valuable and time-consuming submarine surveys that have been conducted in submarine channels (9, 21, 22, 31–33), a significant advantage of surveying in a lacustrine environment (shallow water, low slope) is that direct water–sediment sampling is relatively easy to perform. We collected quasi-spatiotemporally continuous flow velocity and sediment concentration profiles along the turbidity-current pathway in Xiaolangdi Reservoir and conducted bathymetric surveys before, during, and after turbidity current events. We conduct numerical simulations to understand the contributors to current evolution and to better interpret self-acceleration. After confirming the frequent occurrence of SATCs in Xiaolangdi Reservoir with field data and numerical simulations, we further analyze their formative conditions, which refute the previous hypothesis that low-sloping environments cannot produce SATCs (30, 39), and we identify a unified criterion for SATC formation across environments, including low-sloping lakes and reservoirs, laboratory flumes, and both gently and steeply sloping submarine settings. We also discuss the potential application of SATCs for reservoir sedimentation mitigation.

Results

Bathymetric Changes During Turbidity Currents. Bathymetric surveys were conducted using a multibeam echo sounder (MBES) pre- and postflood season and a parametric subbottom sounder (PES) during turbidity-current events. A multibeam system allows rapid mapping of 3D bathymetry via direct scanning of the reservoir bed pre- and postflood season, when incoming flow is relatively clear. However, due to the high concentration of turbidity currents during floods, the acoustic wave emitted from MBES cannot penetrate the dense sediment layer. Instead, we used a PES, which emits a low-frequency component of interfering waves that can penetrate to the bed (operating effectively as a single beam), so post-survey interpolation was needed to obtain 3D reservoir bathymetry during turbidity current events (*Materials and Methods*).

In the 3D bathymetry map of Fig. 1*B*, it is clear that there exists a subaqueous channel beneath the reservoir water, the existence of which was revealed for the first time at Xiaolangdi Reservoir in our 2018 preflood survey. Differing from channel systems widely present in other sublacustrine/marine settings, like the Amazon (48, 49), Congo (50, 51), and Lake Geneva (52), the presence of the channel at Xiaolangdi is intermittent and highly dependent on turbidity-current events (Fig. 1*B* and *SI Appendix*, Figs. S1–S4). The plunging point of a turbidity current coincided roughly with the initiation point of the subaqueous channel (Fig. 1*B* and *SI Appendix*, Fig. S2). The vertical profiles of sediment concentration showed that the stratified structure of turbidity currents was largely retained in the channel, whereas sediment was well mixed vertically on the floodplain-like benches on either side of the channel. As the sediment sluicing gates were shut (during the second half of the flood season) to store water, the reservoir became net-depositional, and a substantial part of the upstream end of the channel was buried and disappeared (*SI Appendix*, Figs. S1*C* and S2 *A* and *C*). Toward the downstream end, however, where turbidity currents remained active (plunging but blocked), the channel persisted (*SI Appendix*, Figs. S1*C* and S2 *A* and *C*).

Massive channel incision was found during occasional powerful turbidity events within the channel (Fig. 1). The thalweg of the subaqueous channel was incised by 5 to 8 m in a single turbidity current event in 2018, and the channel bank abutting the subaqueous benches was undercut by up to ~12 m (Fig. 1 *C*–*F*). The strong erosive power of the turbidity currents can explain the existence of a subaqueous channel and why it remains partially active even when the reservoir becomes net-depositional (*SI Appendix*, Figs. S1*C* and S2 *A* and *C*). The remainder of the reservoir was indeed aggrading, as shown in Fig. 1*C*.

The strong erosive power of these powerful turbidity currents is suggestive evidence for the occurrence of SATC, but nevertheless remains indirect. Direct evidence for SATCs has been established in flume experiments, where sediment concentration and velocity profiles were measured at different longitudinal locations (29, 30). The down-channel variation of total sediment (volume) flux and momentum flux was examined to confirm the existence of SATCs as they strengthen downstream. Here, we use the same standard to check whether the erosive turbidity currents at the Xiaolangdi Reservoir are indeed self-accelerating.

Longitude Variation of Sediment and Momentum Flux. The canonical definition of an SATC requires a positive feedback loop, whereby accelerating flow entrains more sediment, entrained sediment adds to the submerged gravity, and added downslope gravity (force or energy) leads to more acceleration (18–20, 24), thus igniting and sustaining sediment entrainment and long-distance propagation of the turbidity current. This definition does not specify the source of entrained sediment; therefore, material may derive from the channel bed, the bank, or both, as long as it facilitates the acceleration of turbidity currents. In mathematical terms, the material derivative of sediment mass (volume) satisfies $D(HC)/Dt = \partial(HC)/\partial t + \partial(HCU)/\partial x > 0$, and the current

Downloaded from https://www.pnas.org by UNIVERSITY OF ILLINOIS URBANA CHAMPAIGN; BIOLOGY LIB E on May 26, 2026 from IP address 130.126.255.117.

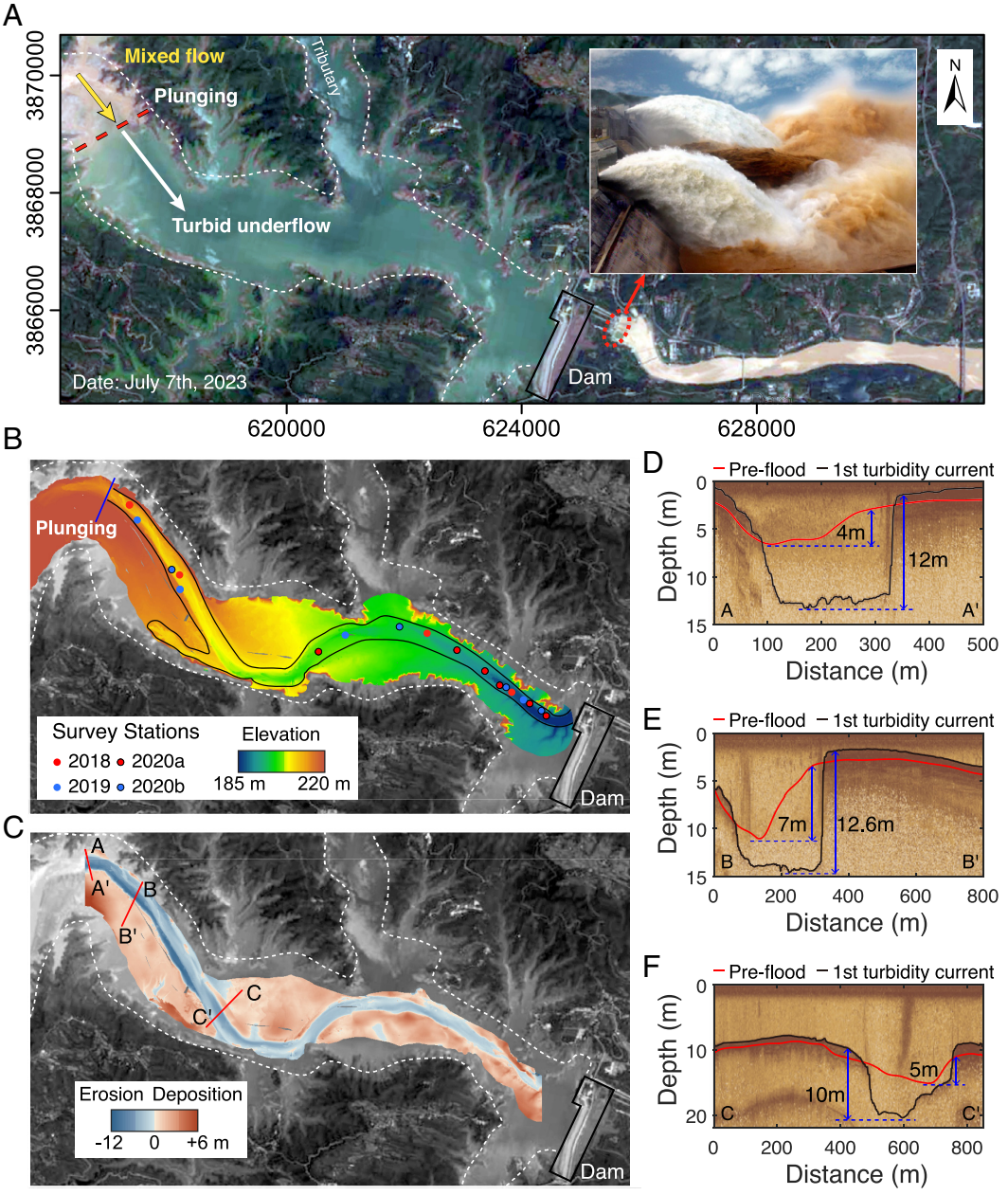

Fig. 1. Map and bathymetry of the Xiaolangdi Reservoir on the Yellow River, China. (*A*) Satellite image of Xiaolangdi Reservoir during a turbidity-current event. The plunging of muddy flow into the *Bottom* of the reservoir is clearly visible. The dam is equipped with sediment-sluicing vents that release sediment downstream from near the base of the dam. (*B*) Bathymetry of Xiaolangdi Reservoir immediately before the 2018 flood season. The bathymetric map reveals a subaqueous channel beneath the reservoir water body, whose initiation point lies close to the plunging line of turbidity currents. (*C*) Bathymetric changes in Xiaolangdi Reservoir during the first turbidity-current event of 2018. Compared with the preflood survey (*SI Appendix*, Fig. S10), the channel was drastically incised (by up to 12 m), while the benches on either side showed clear aggradation. Similar drastic incisions during the first turbidity-current event of the season were also observed in 2019, 2020, and 2023. (*D*–*F*) Cross-section profiles (locations indicated in panel *C*) before the flood and during the peak of the first turbidity-current event of 2018. Channel thalwegs were incised by 5 to 8 m, while some banklines experienced incision of up to ~12 m during this single turbidity-current event.

momentum satisfies $D(HU)/Dt = \partial(HU)/\partial t + \partial(HUU)/\partial x > 0$. Since a natural flood in Xiaolangdi Reservoir may last weeks, the temporal changing rate of sediment-laden flows over each survey period (often half a day) is relatively small and negligible (i.e., $\partial/\partial t \approx 0$). This negligibility is systematically justified in *SI Appendix*, Text S1. Hence, if we can show that $\partial(HCU)/\partial x > 0$ and $\partial(HUU)/\partial x > 0$, that is, downstream increases in sediment volume and layer-momentum flux, we can demonstrate the existence of SATCs at the Xiaolangdi Reservoir.

To confirm this, we controlled each of our down-channel variation surveys to within half a day. The survey scheme is as follows. We first chose multiple survey stations on the water surface above the thalweg of the subaqueous channel, only where turbidity currents were present, to cover as long a distance from the plunging point to the dam site as possible. At each station, we anchored the survey boat and lowered a fish-like weight equipped with four water-sediment samplers and a mechanically propelled velocimeter to multiple points above the bed (*Materials and Methods* and *SI Appendix*, Fig. S5), with the lowest point at ~20 cm above the bed. We used up to three survey boats to take water and sediment samples, measure point velocity, and conduct the bathymetric survey with the PES simultaneously.

Downloaded from https://www.pnas.org by UNIVERSITY OF ILLINOIS URBANA CHAMPAIGN; BIOLOGY LIB E on May 26, 2026 from IP address 130.126.255.117.

During 2018–2020 and 2023, we completed 17 longitudinal survey lines (*SI Appendix*, Extended Data 1). Fig. 2 shows long profiles of the discharges of momentum and suspended sediment during four turbidity current events, and thus allows verification that the flows therein were indeed self-accelerating according to the criteria of $D(HC)/Dt > 0$ and $D(HU)/Dt > 0$. In particular, the turbidity current in 2019 showed increases in sediment volume and momentum flux by factors of ~6 and ~10, respectively, relative to the most upstream measurements. Among the 17 survey lines, nine show segments that clearly satisfy the criteria for self-acceleration, indicating the widespread occurrence of SATCs even in this low-sloping ($S < 0.3\%$) lacustrine environment (38). We also verified that in both $D(HC)/Dt$ and $D(HU)/Dt$ terms (*SI Appendix*, Text S1), the temporal variation rate (i.e., $\partial HC/\partial t$ and $\partial HU/\partial t$) is less than 5% of the spatial variation rates, $\partial(HCU)/\partial x$ and $\partial(HUU)/\partial x$, supporting the neglect of these terms ($\partial/\partial t \approx 0$).

Contributors to the Downstream Acceleration. Multiple other mechanisms other than self-acceleration may lead to simultaneous downstream increases in current sediment and momentum discharges. For instance, according to the governing equation for steady-state current momentum conservation (Eq. **1**), channel-slope increase (S increasing), plunging of the open-channel flow into the turbidity current (constriction of flow or hydrostatic-pressure-gradient drop), and reduction in flow resistance can all boost current momentum, independent of sediment volume increase (i.e., without an increase in CH),

$$\frac{dHUU}{dx} = -\frac{1}{2}Rg\frac{\partial CH^2}{\partial x} + RgCHS - u^{*2}, \qquad [1]$$

where R is specific submerged gravity =1.65 for quartz in water [–], g is gravitational acceleration rate, u^* is the shear velocity $= \sqrt{\tau/\rho}$ where τ is the shear stress and ρ is the fluid density.

We therefore conducted an attribution analysis to examine the contributors to acceleration further. It is worth noting that even when there is no net sediment entrainment, i.e. the bypass condition where entrainment rate equals deposition rate, the momentum discharge of the current can still increase due to thickening of the current layer (H) (53). A fair baseline for assessing whether sediment entrainment plays a role in acceleration is a flow over a constant slope (S_0) under the bypass condition (53), but otherwise sharing the same initial and boundary conditions as the Xiaolangdi turbidity currents.

Eq. (**2**) below assesses the contributors to the increment in momentum acceleration relative to the bypass case.

$$\Delta\overline{\frac{dHUU}{dx}} = \overline{\frac{dHUU}{dx}}_{erodible} - \overline{\frac{dHUU}{dx}}_{bypass} = -\frac{1}{2}Rg\Delta\frac{\partial CH^2}{\partial x} + RgS_0\Delta(CH) + Rg(CH)_0\Delta S + Rg\Delta S\Delta(CH) - \Delta u^{*2}. \qquad [2]$$

In the bypass case, a constant slope regressed from the actual channel longitudinal profile observed at Xiaolangdi, was used for the comparison. Hence, the contribution of relative changes in plunging (hydrostatic pressure gradient term), slope (S), and sediment volume (CH) in the current can be examined via Eq. (**2**). Since surveying near the plunging point was unsafe, we could obtain only limited observations to quantify the contribution of plunging to acceleration. We thus used a RANS (k–ε) numerical model (10) to incorporate and evaluate the effect of plunging on acceleration (*Materials and Methods* and *SI Appendix*, Figs. S6–S8).

Fig. 3 shows the results of the attribution analysis of the 2019 event. It clearly demonstrates that the sediment entrainment term contributes the most to the flow acceleration ~250% of the net acceleration rate increment, while plunging (hydrostatic term in Fig. 3) contributes only locally (*SI Appendix*, Fig. S8*C*) and overall, relatively little (–31 to 64%). Friction most strongly opposes flow acceleration (–170% of the net acceleration rate increment), and the other terms, including slope change, contribute minimally. The attribution analysis clearly shows that sediment entrainment plays the dominant role in flow acceleration, confirming that the turbidity current in the Xiaolangdi Reservoir self-accelerates and

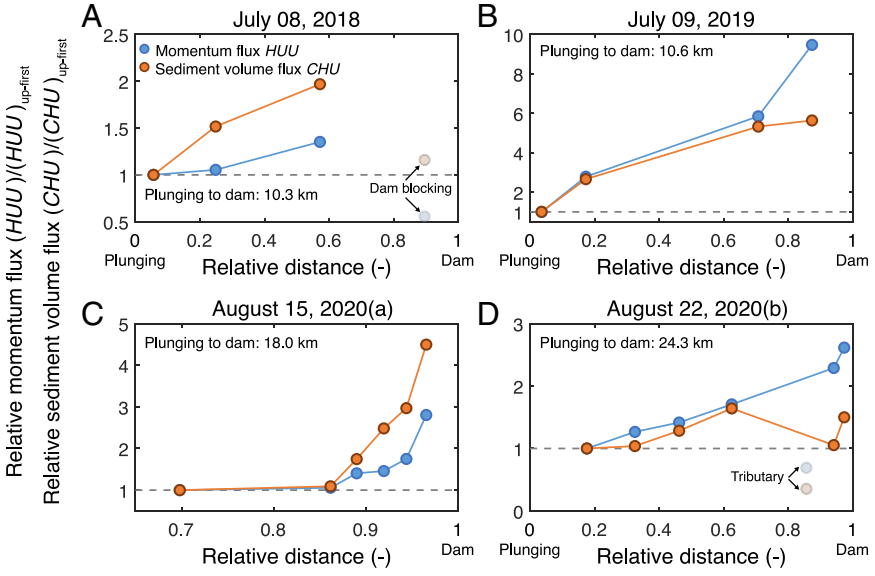

Fig. 2. Spatial variation of sediment volume flux and turbidity-current momentum flux along the subaqueous channel. Spatial variations of sediment volume flux and turbidity-current momentum flux along the pathway of turbidity events are relative to the measured point farthest upstream. In all four panels *A*–*D*, clear downstream increases in suspended-sediment mass (volume) and momentum discharges per unit width provide direct evidence of sediment entrainment and acceleration of turbidity currents as they propagate, providing a rigorous criterion for identifying SATCs. While turbidity currents self-accelerate throughout in *B* and *C*, a significant dam blocking effect, due to the low openness of the sluicing gate, was observed and the turbidity current was reflected by the dam and formed a lutocline that reduced sediment concentration and velocity remarkably in *A*; in *D*, the tributary north of the reservoir (Fig. 1*A*) input clear water flow that diluted and diverted the turbidity current, reducing both local concentration and down-channel flow velocity.

Downloaded from https://www.pnas.org by UNIVERSITY OF ILLINOIS URBANA CHAMPAIGN; BIOLOGY LIB E on May 26, 2026 from IP address 130.126.255.117.

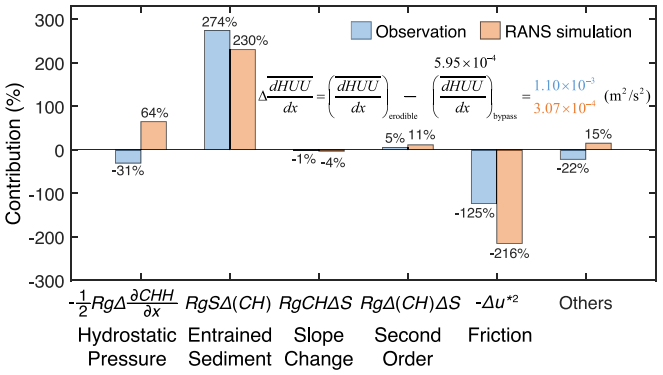

Fig. 3. Attribution analysis of the increased momentum-acceleration rate. Momentum acceleration can occur without sediment entrainment (e.g., under bypass conditions), and thus does not necessarily represent self-acceleration. True self-acceleration is achieved only when sediment entrainment is the dominant contributor to acceleration. We therefore compare the 2019 field observations with a baseline reference, a turbidity current under bypass conditions, and analyze the surplus momentum-acceleration rate $\Delta[d(HUU)/dx]$. The analysis shows that sediment entrainment accounts for approximately 274% of the surplus momentum acceleration, despite substantial offset from friction, while channel slope, hydrostatic pressure, and other terms contribute minimally. It is worth noting that plunging of an open-channel sediment-laden flow into a turbidity current is widely known to locally accelerate the current; however, our 2019 field data did not include observations upstream of the plunging point to evaluate its contribution. Therefore, a two-fluid RANS model (10) (k–ϵ) was used to simulate the turbidity current so as to incorporate the plunging process, as detailed in the *Materials and Methods*. The RANS results confirm an increase in the plunging-induced contribution via the hydrostatic-pressure term, although this contribution remains much smaller than that of sediment entrainment.

that powerful SATCs can frequently occur in a low-sloping lacustrine environment.

With SATCs confirmed, we can further attribute the source of eroded sediment that fuels SATCs, via detailed bathymetric change analyses (*SI Appendix*, Text S2). These analyses demonstrate that more than 85% of the total sediment erosion, fueling SATCs, originates from the channel bed, whereas bank erosion contributed less than 12% of the total eroded material. This attribution is consistent with observations in submarine channels, where sediment erosion was found to originate predominantly from bed incision, exceeding 90% in a muddy system (Cango Canyon) (54) and approximately 80% in a sand-bed system (Bute Inlet, Canada) (55), indicating that vertical bed incision, rather than lateral expansion, is the primary mechanism sustaining the self-accelerating nature of these currents.

Notably, several other potential contributors, including temporal variations of upstream boundary conditions (e.g., inflow discharge and sediment concentration), reservoir water level fluctuations, and sediment sluice gate operations, are not explicitly discussed. This exclusion is justified because our evaluations show that the relative changes in these factors are minimal during each survey period (*SI Appendix*, Table S2). In particular, opening the bottom sluice gate is hypothesized to generate a suction effect that could accelerate turbidity currents. However, the free streamline theory (56, 57) predicts that suction-induced effects upstream of a constriction are highly localized; in this instance, they are confined to within 50-200 m of the dam (*SI Appendix*, Text S3), whereas SATCs can form 10-20 km upstream from the dam (e.g., Fig. 2). Furthermore, as discussed in *SI Appendix*, Text S3, SATCs can still form (Fig. 2*A*) and produce massive in-channel erosion (Fig. 1 *D*–*F*) even when the sluice gate is closed and the floodplain is a depositional environment. This substantiates that the suction effect from the sediment sluice gate is not the primary driver for the turbidity current acceleration. Below, we further extend our discussion on the formative conditions for SATCs.

Discussion

Low-sloping environments, corresponding to Froude-subcritical conditions (38), were often not perceived to support SATCs, as they do not readily facilitate the formation of fast currents (9, 30, 39, 58). Indeed, the maximum velocity of turbidity currents observed in Xiaolangdi Reservoir was ~3.7 m/s, well below some measured values (>5 m/s) in steep-sloping submarine channels (9). Previously documented SATCs, such as those in flume setups (30), were all Froude-supercritical and in steep channels (Fig. 4*A*). Our observations at Xiaolangdi, however, refute the idea that SATCs require Froude-supercritical flow: 62% of recorded SATC events (with criteria of $D(HC)/Dt > 0$ and $D(HU)/Dt > 0$) are Froude-subcritical (Fig. 4*A*). Therefore, Froude supercriticality is not a necessary condition for the formation of SATC.

To explore the formative condition for SATC, we invoke the early energy balance theory (19, 20, 24, 25), which proposed the Knapp-Bagnold number, US/v_s, as a criterion, where U is the layer-averaged current velocity, S is the channel slope and v_s is the sediment settling velocity. In order to consider the nonuniform grain size distribution of the suspended sediment in a turbidity current, we derive a modified Knapp-Bagnold number as follows. Consider an equilibrium turbidity current. The unit power it converts from gravitational energy to turbulent kinetic energy and later to the friction-induced heat is $P_f = RgCHSU$. The energy needed to keep the sediment in suspension is $P_s = RgCHv_s$. Hence, the conventional criterion was obtained by letting $P_f > P_s$, yielding $US > v_s$. If the suspended sediment is nonuniform, keeping all sizes within a range in suspension requires $P_f > P_s$, where $P_s = \Sigma P_{si} = \Sigma RgHC_iv_{si}$. This in turn gives the criterion $US > v_{sr}$ where $v_{sr} = \Sigma C_iv_{si}/C = \int v_s(D)f(D)\mathrm{d}D$ and $f(D)$ is the probability distribution function of the suspended sediment grain size. Thus, v_{sr} is seen to be the arithmetic average settling velocity, weighted by its composition. For consistency below, we use $US > v_s$ to be consistent throughout, where v_s is used as shorthand for v_{sr}.

Bagnold (24) and Parker (19) argued that the threshold condition for the formation of SATC is when $US/v_s > 1$. Pantin (20) suggested $US/v_s >> 1$ (~100) to form SATC's. Parker et al. (27) further argued $US/v_s > 1$ is only a necessary condition and recommended using a numerical model to identify its formative condition. However, adopting a numerical model for SATC identification (58, 59) obviously requires much more information and work than just using a single value of US/v_s. Previous field (21) and flume observations (29) showed that $US/v_s > 1$ was indeed satisfied for accelerating currents, but the exact threshold was neither well tested nor constrained, due to data scarcity.

We augmented our observations in 2018–2023 by further compiling historical data observed from Xiaolangdi for 2005–2017 (*Materials and Methods*). The historical data have a relatively low spatial resolution and are hardly continuous (e.g., sometimes only two survey stations in one event). The data were therefore selected according to the following criteria. First, the data were surveyed in the center of the subaqueous channel. Second, there were at least two profiles in the longitudinal direction to tell whether the flow is erosive or depositional (DHC/Dt) and whether it was accelerating or decelerating (DHU/Dt). Third, the profiles were collected in half a day (minimal temporal change). Fourth, the surveyed profiles were sufficiently far upstream from the dam to avoid dam impacts such as current reflection. We use the criteria $DHC/Dt > 0$ and $DHU/Dt > 0$ to identify SATC segments, and $DHC/Dt < 0$ and $DHU/Dt < 0$ to select segments where the current

Downloaded from https://www.pnas.org by UNIVERSITY OF ILLINOIS URBANA CHAMPAIGN; BIOLOGY LIB E on May 26, 2026 from IP address 130.126.255.117.

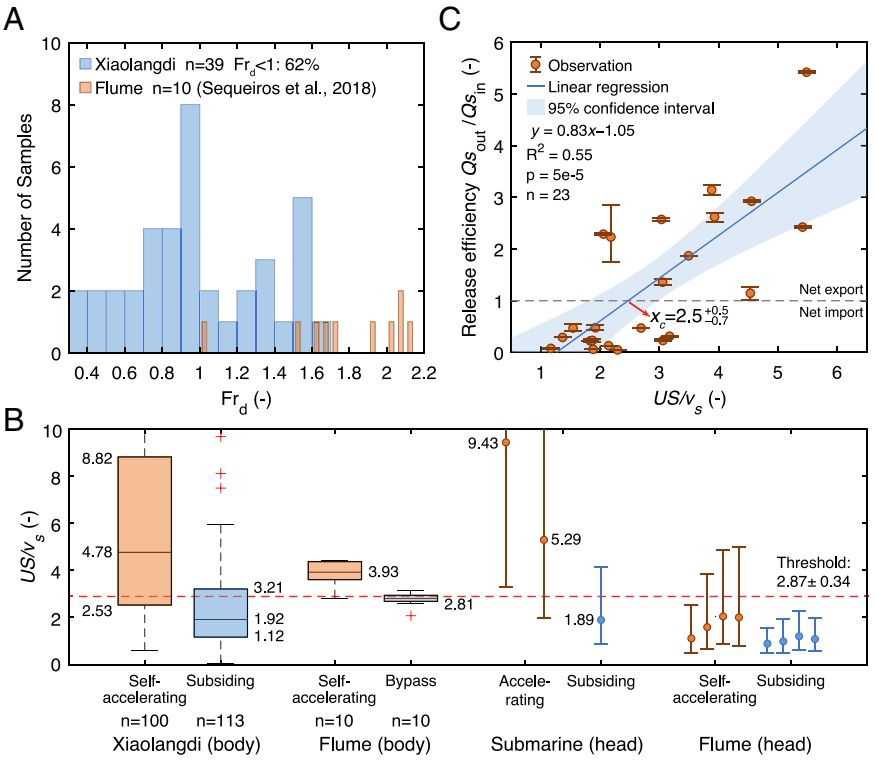

Fig. 4. Formative condition for SATCs and their application to mitigation of reservoir sedimentation. (*A*) Densimetric Froude number (Fr_d) of SATCs. Low-slope, Froude-subcritical conditions were long perceived as unfavorable for the formation of SATCs (9, 30, 39, 58), which is why lacustrine environments (characterized by low slope and low Fr_d) were not traditionally considered ideal for SATC development. However, data from Xiaolangdi Reservoir show otherwise: SATCs occur frequently under Froude-subcritical conditions. (*B*) The modified Knapp–Bagnold numbers US/v_s of different types of turbidity currents across various environments. A threshold Knapp–Bagnold number of approximately 2.87 ± 0.34 can be identified from the Xiaolangdi data, separating SATCs (US/v_s>threshold) from subsiding ones (US/v_s<threshold). The threshold derived from the lacustrine Xiaolangdi environment also serves as a general criterion for both laboratory-scale flume experiments (29, 30) and field-scale submarine turbidity currents (9) (see also *SI Appendix*, Fig. S9). (*C*) Relationship between reservoir sediment-release efficiency and the modified Knapp–Bagnold number. As theoretically predicted and evidenced in Fig. 1, SATCs can not only export the sediment they carry but also erode and export previously deposited reservoir sediment (sediment release efficiency > 1). The positive correlation between sediment-release efficiency and our modified Knapp–Bagnold number further supports this conclusion. Notably, turbidity currents achieve net sediment export precisely when the threshold identified in *B* is crossed, above which SATCs are expected to occur. This indicates their dominant role in driving sediment exports from the reservoir. Therefore, it is reasonable to expect that the Knapp–Bagnold threshold (2.87 ± 0.34) generally corresponds to the onset of potential net sediment export conditions (sediment-release efficiency > 1) in various reservoir environments, where the potential needs to be realized by opening sluice gates at the bottom of the dam.

subsides, with each segment containing at least two points. We then used spatially average values of US/v_s to evaluate tendencies for self-acceleration or subsidence.

Fig. 4*B* shows the threshold value of US/v_s that we identified in the Xiaolangdi data, illustrating a systematic difference between self-accelerating and subsiding currents. Most SATCs (over 75%) satisfy $US/v_s > 2.53$, and most subsiding currents (over 75%) satisfy $US/v_s < 3.21$. The threshold for SATC's is thus narrowed down to between 2.53 and 3.21 (2.87 ± 0.34), which is greater than Bagnold-Parker threshold (unity) but much less than Pantin's (100). Interestingly, this threshold, developed from the low-sloping lacustrine environments, also applies to the steep-sloping flumes and submarine settings. Both flume and submarine currents can be separated correctly by the above criterion into SATC's on the one hand, and subsiding or bypass flows on the other hand (Fig. 4*B*). It is worth noting that the values of US/v_s at the head of SATCs in the flume setting are below the threshold. This can be explained by the fact that in a flume setting, the turbidity current head (and body) is pushed and sustained by the upstream, continuous sediment-laden flow input, just like the ones observed in the Xiaolangdi reservoir. This was evidenced by flume experiments where the body velocity is greater than the head (30). Therefore, it is reasonable to use the Knapp-Bagnold number in the body of the current as the indicator for SATC. However, the majority of submarine turbidity currents are led by a dense, rapid, sometimes accelerating head (1, 9), and the body instead follows the head at a lower velocity; hence, the head Knapp-Bagnold number should be used to examine the propagating status. In the field cases of submarine currents, only cases with measured grain size distributions of suspended sediment were used, and such cases were very limited (Fig. 4*B*). We present results for other recorded accelerating and decelerating cases, including those in Gaoping, Congo, and Monterey canyons and Bute Inlet (9), where only sand and mud proportions were estimated in *SI Appendix*, Fig. S9, whereby sensitivity analysis on the sand size indicates that the threshold outlined above works for these cases as well. We therefore conclude that a relatively low settling velocity v_s of the suspended sediment (corresponding to fine grain size) in the incoming flow, along with the powerful initial current velocity (large U) of that flow, may be the primary controls on the formation of SATC's in a low-sloping lacustrine environment, based on the criterion of $US/v_s > 2.87 \pm 0.34$.

Considering the strong erosive nature of SATCs, we propose that SATCs can be used to manage reservoir sedimentation, as they can not only export all their own sediment through the dam but also erode and export sediment previously deposited in the reservoir (Fig. 2). Despite the wide application of turbidity currents for the mitigation of reservoir sedimentation (17), the role of self-acceleration, i.e., net export of sediment rather than import, has seldom been emphasized. This is likely because the erosiveness of SATCs has rarely been evaluated at the flood-event scale, largely because reservoir bathymetry surveys were inefficient and costly until relatively recently. With our observations and the data compiled under the criteria developed with our observations, we can assess the efficiency of sediment release via sluicing from the dam during a turbidity current. We show that the sediment release efficiency (ratio of output sediment to input Q_{s_out}/Q_{s_in}) is proportional to the modified Knapp-Bagnold number (Fig. 4*C*). Specifically, a turbidity current can become a net exporter of sediment via the opening of sluice gates when the Knapp-Bagnold number exceeds $2.5^{+0.5}_{-0.7}$, consistent with our SATC threshold (2.87 ± 0.34). It is worth mentioning that the positive relation between sediment release efficiency and SATCs may depend strongly on the upstream sediment and water discharge conditions, fine sediment availability, reservoir geometry, water level, and the degree to which sluice gates at the dam are opened. Therefore, with several site-specific uncertainties, the functional form of the relation may vary from one reservoir to

Downloaded from https://www.pnas.org by UNIVERSITY OF ILLINOIS URBANA CHAMPAIGN; BIOLOGY LIB E on May 26, 2026 from IP address 130.126.255.117.

another; however, it is reasonable to predict that a given flow will pass the net-export threshold at roughly the same Knapp-Bagnold number (2.87 ± 0.34). This threshold provides general guidance on what to control to engineer SATCs in reservoir systems to mitigate reservoir sedimentation, restore sediment connectivity, and support sustainable river engineering projects.

In this study, we report on a four-year program of field surveys of turbidity currents in Xiaolangdi Reservoir. This reservoir is on the world's most dense sediment-laden river, the Yellow River, China. We present clear evidence that SATCs in Xiaolangdi Reservoir occur frequently. SATCs eroded the reservoir sediment significantly (5 to 12 m incision during one event) and led to the net-export of sediment through the dam. The observations of SATCs at the low-slope, Froude-subcritical, lacustrine environments refute the hypotheses that SATCs can only occur in the steep channels (39) or under high velocity conditions (9). We use field data to identify the threshold value for SATCs with a modified Knapp-Bagnold number ($US/v_s > 2.87 \pm 0.34$) that applies not only to the turbidity currents in the low-slope Xiaolangdi Reservoir but also to steep flume and submarine settings. It can therefore be derived that the occurrence of SATC in the low-sloping lacustrine setting (small S) relies on high initial velocity and fine-grained sediment of the turbidity current. We show that the criterion for the formation of SATCs can be applied to engineer net-erosive conditions for reservoir management, so as to mitigate reservoir sedimentation, restore sediment connectivity between the upstream and downstream sides of the dam, and help develop sustainable river engineering projects.

Materials and Methods

Bathymetry Survey. Comprehensive 3D Bathymetric surveys were carried out, before, during, and after turbidity current events (see *SI Appendix*, Fig. S10 for survey date and corresponding water and sediment conditions). During nonflood periods, when incoming flow is relatively clear (low sediment concentration), the 3D bathymetry was mapped with an R2Sonic multibeam echo sounder MBES. These surveys were conducted prior to and following flood seasons in 2018–2020, and in 2023, we performed pre- and post-first-flood surveys to capture event-scale bathymetric changes. High-resolution positioning and motion data were provided by an RTK GPS and an inertial measurement unit (IMU), which complemented the MBES system's antennas. Vertical resolution was maintained within 5 cm, with primary uncertainties arising from RTK-based elevation measurements of the moving vessel, while horizontal resolution exceeded approximately 1 cm due to the high-precision RTK system (see *SI Appendix*, Fig. S5 for equipment arrangement on the vessel).

During turbidity-current events, the high sediment concentration prevented MBES acoustic waves from penetrating the dense flow layer, making full 3D mapping infeasible. To overcome this limitation, an Innomar parametric subbottom sounder (PES) was employed as a single-beam system to record point-depth measurements along the vessel's track. The survey vessel followed a zigzag trajectory across the subaqueous channel to ensure complete spatial coverage. This navigation pattern, combined with subsequent interpolation, enabled the reconstruction of bathymetry during turbidity-current conditions.

Water-Sediment and Velocity Survey. Mechanical current velocimeter and Van-Dorn-style suspended sediment samplers were mounted to a fish-like weight (called a *lead fish)* to be deployed underwater to collect velocity and sediment samples (*SI Appendix*, Fig. S5). The weight is approximately 100 kg to ensure a stable vertical entry into the water and features a streamlined, fish-like design that naturally aligns with the main flow direction. At the head of the weight, a propeller-type current meter was mounted, while the body at the same elevation integrated four Van-Dorn-style suspended sediment samplers and a pressure sensor. The current meter recorded point-averaged flow velocity; the samplers collected water–sediment samples; and the pressure sensor provided precise depth for each sampling point.

The measurement protocol was as follows: Within the real-time identified subaqueous channel, multiple (at least three) survey stations were positioned along the flow direction, and all sampling operations were completed within half a day. Upon arrival at a target station, the survey vessel anchored and deployed the fish-like weight. During each deployment, the four Van-Dorn-style sediment samplers collected samples sequentially at different depths, after which the weight was retrieved to the deck for sample recovery. Velocity data from the propeller-type current meter were transmitted in real time. Visual inspection of sediment concentration differences in the samples provided a preliminary estimate of the interface between the clear-water layer and the turbid layer. Sampling intervals in the clear-water layer were approximately 4 m, while intervals within the turbid layer were progressively reduced with depth, averaging about 1.4 m, until the weight reached the bed. Due to the instrument's size, the lowest sampling point corresponded to approximately 0.2 m above the bed surface (*SI Appendix*, Fig. S5).

During measurements, the current meter was held stationary for 40 to 60 s at each point, and each sediment sampler collected no less than 500 ml per sample. Collected samples were analyzed for sediment concentration using oven-drying and weighing, and grain-size distribution was determined by laser diffraction. Pressure-sensor data were time-stamped and converted to corresponding sampling depths. Ultimately, 17 quasi-continuous longitudinal profiles were obtained, with an average of 5.06 stations per longitudinal profile and an average station spacing of 1.62 km.

For each vertical profile of flow velocity and sediment concentration, the turbidity current thickness H, depth-averaged velocity U, and concentration C are defined per Ellison and Turner (60) and Parker et al. (18) as follows. $U = \int_0^{h_u} u^2(z)dz / \int_0^{h_u} u(z)dz, H = \int_0^{h_u} u(z)dz/U$ and $C = \int_0^{h_u} u(z)c(z)dz/(HU)$; however, their integration range is from bed (z=0) to an upper bound of the turbidity current layer (h_u), where h_u is defined as the 95th percentile location for the sediment flux above the peak flux (see *SI Appendix*, Figs. S11 and S12 for details), differing from the original free-surface method ($h_u \to \infty$) proposed in Ellison and Turner (60) and Parker et al. (18). The reason for applying the finite upper bound instead of the free-surface method is that the free-surface method is only feasible for small-scale, controlled conditions like flume experiments. On larger scales inherent with natural settings (e.g., lakes, reservoirs, fjords, and oceans), turbidity currents are not the only mechanism that potentially drives the current; for example, surface/internal waves and currents, tidal currents, and/or reservoir operations (e.g., spillway water release) all can potentially produce nonzero velocities, biasing the result obtained via the free-surface method. We compare different definition methods to see their impacts on our results in *SI Appendix*, Text S4. The layer-averaged sediment grain size distribution of the turbidity current was obtained by the concentration-weighted, depth-averaged sediment grain size, which is later used for settling velocity estimation.

Numerical Simulations.

Two-fluid Reynolds-Averaged Navier–Stokes (RANS) k-ε model. We implemented a two-fluid RANS model (10), previously adapted for simulating hyperpycnal flows in river estuaries. To capture the self-accelerating behavior of turbidity currents, sediment entrainment suitable for Xiaolangdi reservoir was incorporated into the model. Because the sediment supplied from the upstream loess plateau and deposited in the reservoir consists primarily of fine silt (median grain size ~13 μm), we adopted an entrainment function derived from the Generalized Engelund–Hansen theory (61, 62), which is developed explicitly for silt-rich sediment transport:

$$E_s^* = \frac{\alpha(\tau^*)^{n-1.5} r_0 S}{R\sqrt{C_f}},$$

where E_s^* dimensionless entrainment rate, r_0 is the ratio of sediment concentration at bed reference height to the depth-averaged [r_0 =7.5 according to field measurements (63)], n = 5/3, α = 0.9, C_f is resistance coefficient (~0.0015), R = 1.65 is sediment submerged specific gravity, dimensionless shear stress τ^* is obtained from the numerical simulation, D is the representative grain size.

Numerical simulations were performed for the turbidity-current event in 2019. To simulate the plunging process, the computation began with an open channel sediment-laden flow, which later plunged to form turbidity currents automatically, and the upstream open channel boundary condition is tuned

Downloaded from https://www.pnas.org by UNIVERSITY OF ILLINOIS URBANA CHAMPAIGN; BIOLOGY LIB E on May 26, 2026 from IP address 130.126.255.117.

to match the first profile after plunging with the observed data. The computational domain consisted of 1,024 grid cells in the downstream direction and 196 cells in the vertical direction, respectively. Vertical resolution was refined near the bed, with grid spacing increasing upward at a stretching ratio of 1.025. Consequently, the dimensionless wall distance (y^+) of the first grid was 158, which falls within the recommended range (30 to 300) for applying wall functions.

The model successfully reproduced the plunging of this flow into a turbidity current and its subsequent evolution. Downstream propagation patterns are presented in *SI Appendix*, Fig. S6 and compared against field measurements in *SI Appendix*, Fig. S7. Moreover, the contribution of each source term to momentum acceleration is shown in *SI Appendix*, Fig. S8.

Layer-averaged turbidity current model with bypass conditions. To conduct attribution analysis, we employ the layer-averaged turbidity current model (18) to simulate the 2019 turbidity current event, whereby the upstream boundary condition used the first observation downstream of the plunging point. The simulation is meant to provide a reference value for the momentum acceleration, as the momentum flux can still increase downstream without sediment entrainment due to current-layer thickening. The bypass condition imposed zero sediment entrainment along the path, and therefore, the sediment flux per unit width $q_{s_up} = (UCH)_{up} = 0.0216\ \mathrm{m}^2/\mathrm{s}$ is a constant. The upstream condition for discharge per unit width is $q_{w_up} = (UH)_{up} = 2.24\ \mathrm{m}^2/\mathrm{s}$. The constant slope S_0=0.0041 and D=16 μm were derived from the 2019 survey. We implemented the ambient water entrainment function based on flume experiments (64); however, since it has substantial uncertainty, we calibrated the function (64) with our field data and found that a correction factor of 0.4 is needed to reproduce the layer thickening process accurately. The resistance coefficient is obtained from the RANS model C_f=0.0021.

Compilation of Historical Data From Xiaolangdi Reservoir. We compiled historical turbidity-current survey data collected by the local hydrological department between 2005 and 2017. These records include vertical profiles of flow velocity and sediment concentration at various times and locations. To ensure spatiotemporal continuity, each longitudinal profile selected from the historical dataset contained at least three survey stations, and the total duration of measurements across all stations within a profile was less than four hours. Applying these criteria, we obtained 84 longitudinal profiles, although their spatial resolution was considerably lower than that of our recent surveys. For analysis, two adjacent profiles were grouped as a segment to evaluate whether the flow exhibited self-acceleration or subsidence. Ultimately, 61 segments were classified as self-accelerating and 93 as subsiding.

Data, Materials, and Software Availability. All study data are included in the article and/or supporting information.

ACKNOWLEDGMENTS. We thank Huaibao Ma and Yuanfeng Zhang for their unselfish sharing of their knowledge on Xiaolangdi turbidity currents. Andrew Moodie's participation in the field survey is appreciated. We thank Michael Lamb for his comments that inspired the attribution analysis. We are grateful to Gary Parker for the rich discussions. We thank the editor, Octavio Sequeiros, and an anonymous reviewer for their insightful reviews. G.D., X.C., Y.Z., and X.F. acknowledge the support of the NSFC grant via No. U2340223. Y.W. acknowledges the support from NSFC via No. U2243241. M.C. acknowledges the support of Royal Society Research Fellowship DHF\R1\180166.

Author affiliations: [a]Department of Hydraulic Engineering, Tsinghua University, Beijing 100084, China; [b]Department of Civil and Environmental Engineering, Ven Te Chow Hydrosystems Laboratory, The Grainger College of Engineering, University of Illinois at Urbana-Champaign, Urbana, IL 61801; [c]Yellow River Institute of Hydraulic Research, Key Laboratory of the Yellow River, Zhengzhou 450003, China; [d]Department of Geology and Geophysics, University of Wyoming, Laramie, WY 82071; [e]Department of Geosciences, Texas Tech University, Lubbock, TX 79409; [f]Department of Civil Engineering, Hokkaido University, Sapporo, Hokkaido 060-0808, Japan; and [g]Department of Geography, Durham University, Durham DH1 3LE, United Kingdom

Author contributions: H.M. designed research; H.M., G.D., X.C., Y.W., B.M., J.N., Y.Z., and T.I. performed research; G.D., B.M., and T.I. contributed new reagents/analytic tools; G.D. compiled, curated, and visualized the data; H.M., G.D., Y.Z., and X.F. analyzed data; H.M., Y.W., and X.F. administered the project; H.M., Y.W., and X.F. acquired funding; H.M. wrote the first draft of the paper; and all authors contributed to the writing.

1. P. J. Talling *et al.*, Detailed monitoring reveals the nature of submarine turbidity currents. *Nat. Rev. Earth Environ.* **4**, 642–658 (2023).
2. P. Chen *et al.*, Direct evidence that microplastics are transported to the deep sea by turbidity currents. *Environ. Sci. Technol.* **59**, 7278–7287 (2025).
3. F. Pohl, J. T. Eggenhuisen, I. A. Kane, M. A. Clare, Transport and burial of microplastics in deep-marine sediments by turbidity currents. *Environ. Sci. Technol.* **54**, 4180–4189 (2020).
4. I. A. Kane *et al.*, Seafloor microplastic hotspots controlled by deep-sea circulation. *Science* **368**, 1140–1145 (2020).
5. Y. Yang *et al.*, How does plastic litter accumulate in submarine canyons?. *Geophys. Res. Lett.* **51**, e2024GL110767 (2024).
6. P. J. Talling *et al.*, The global turbidity current pump and its implications for organic carbon cycling. *Annu. Rev. Mar. Sci.* **16**, 105–133 (2024).
7. L. P. Bailey *et al.*, Preconditioning by sediment accumulation can produce powerful turbidity currents without major external triggers. *Earth Planet. Sci. Lett.* **562**, 116845 (2021).
8. M. L. Baker *et al.*, Globally significant mass of terrestrial organic carbon efficiently transported by canyon-flushing turbidity currents. *Geology* **52**, 631–636 (2024).
9. P. J. Talling *et al.*, Longest sediment flows yet measured show how major rivers connect efficiently to deep sea. *Nat. Commun.* **13**, 4193 (2022).
10. T. Iwasaki, G. Parker, The role of saltwater and waves in continental shelf formation with seaward migrating clinoform. *Proc. Natl. Acad. Sci. U.S.A.* **117**, 1266–1273 (2020).
11. Bute Inlet, Congo Fan, Decadal architecture and morphodynamics of modern, river–fed turbidite systems. *J. Sediment. Res.* **95**, 104–132 (2025).
12. P. P. E. Weaver, J. Thomson, Calculating erosion by deep-sea turbidity currents during initiation and flow. *Nature* **364**, 136–138 (1993).
13. A. Wahab, D. C. Hoyal, M. Shringarpure, K. M. Straub, A dimensionless framework for predicting submarine fan morphology. *Nat. Commun.* **13**, 7563 (2022).
14. M. A. Clare *et al.*, Volcanic eruptions and the global subsea telecommunications network. *Bull. Volcanol.* **87**, 51 (2025).
15. M. A. Clare *et al.*, Fast and destructive density currents created by ocean-entering volcanic eruptions. *Science* **381**, 1085–1091 (2023).
16. M. Azpiroz-Zabala *et al.*, Newly recognized turbidity current structure can explain prolonged flushing of submarine canyons. *Sci. Adv.* **3**, e1700200 (2017).
17. S. Chamoun, G. D. Cesare, A. J. Schleiss, Managing reservoir sedimentation by venting turbidity currents: A review. *Int. J. Sediment Res.* **31**, 195–204 (2016).
18. G. Parker, Y. Fukushima, H. M. Pantin, Self-accelerating turbidity currents. *J. Fluid Mech.* **171**, 145–181 (1986).
19. G. Parker, Conditions for the ignition of catastrophically erosive turbidity currents. *Mar. Geol.* **46**, 307–327 (1982).
20. H. M. Pantin, Interaction between velocity and effective density in turbidity flow: Phase-plane analysis, with criteria for autosuspension. *Mar. Geol.* **31**, 59–99 (1979).
21. C. J. Heerema *et al.*, What determines the downstream evolution of turbidity currents? *Earth Planet Sci. Lett.* **531**, 116023 (2020).
22. C. K. Paull *et al.*, Powerful turbidity currents driven by dense basal layers. *Nat. Commun.* **9**, 4114 (2018).
23. E. L. Pope, A. Normandeau, C. O. Cofaigh, C. R. Stokes, P. J. Talling, Controls on the formation of turbidity current channels associated with marine-terminating glaciers and ice sheets.. *Mar. Geol.* **415**, 105951 (2019).
24. R. A. Bagnold, Auto-suspension of transported sediment; turbidity currents. *Proc. R. Soc. Lond. A Math. Phys. Sci.* **265**, 315–319 (1962).
25. R. T. Knapp, Energy-balance in stream-flows carrying suspended load. *Eos Trans. Am. Geophys. Union* **19**, 501–505 (1938).
26. H. Vlugter, Sediment transport by running water. *De Ingenieur van Nederlands Indie* **8**, 139–147 (1942).
27. Y. Fukushima, G. Parker, H. M. Pantin, Prediction of ignitive turbidity currents in Scripps Submarine-Canyon. *Mar. Geol.* **67**, 55–81 (1985).
28. M. Garcia, *Sedimentation Engineering: Processes, Measurements, Modeling, and Practice* (ASCE, 2008).
29. O. E. Sequeiros, H. Naruse, N. Endo, M. H. Garcia, G. Parker, Experimental study on self-accelerating turbidity currents. *J. Geophys. Res. Oceans* **114**, 2008JC005149 (2009).
30. O. E. Sequeiros, R. Mosquera, F. Pedocchi, Internal structure of a self-accelerating turbidity current. *J. Geophys. Res. Oceans* **123**, 6260–6276 (2018).
31. L. Carter, J. D. Milliman, P. J. Talling, R. Gavey, R. B. Wynn, Near-synchronous and delayed initiation of long run-out submarine sediment flows from a record-breaking river flood, offshore Taiwan. *Geophys. Res. Lett.* **39**, 2012GL051172 (2012).
32. R. Gavey *et al.*, Frequent sediment density flows during 2006 to 2015, triggered by competing seismic and weather events: Observations from subsea cable breaks off southern Taiwan. *Mar. Geol.* **384**, 147–158 (2017).
33. E. L. Pope *et al.*, First source-to-sink monitoring shows dense head controls sediment flux and runout in turbidity currents. *Sci. Adv.* **8**, eabj3220 (2022).
34. S. M. Simmons *et al.*, Novel acoustic method provides first detailed measurements of sediment concentration structure within submarine turbidity currents. *J. Geophys. Res. Oceans* **125**, e2019JC015904 (2020).
35. J. Peter, C. K. Talling, D. J. W. Paull, Piper, How are subaqueous sediment density flows triggered, what is their internal structure and how does it evolve? Direct observations from monitoring of active flows. *Earth-Sci. Rev.* **125**, 244–287 (2013).
36. J. A. Covault, A. Fildani, B. W. Romans, T. McHargue, The natural range of submarine canyon-and-channel longitudinal profiles. *Geosphere* **7**, 313–332 (2011).
37. F. Pohl, J. T. Eggenhuisen, M. Tilston, M. J. B. Cartigny, New flow relaxation mechanism explains scour fields at the end of submarine channels. *Nat. Commun.* **10**, 4425 (2019).
38. O. E. Sequeiros *et al.*, Regimes of bedforms created by down-slope density currents. *Earth-Sci. Rev.* **272**, 105322 (2025).

Downloaded from https://www.pnas.org by UNIVERSITY OF ILLINOIS URBANA CHAMPAIGN; BIOLOGY LIB E on May 26, 2026 from IP address 130.126.255.117.

39. H. M. Pantin, M. C. Franklin, Predicting autosuspension in steady turbidity flow: Ignition points and their relation to Richardson numbers. *J. Sediment. Res.* **79**, 862–871 (2009).
40. S. Wang *et al.*, Reduced sediment transport in the Yellow River due to anthropogenic changes. *Nat. Geosci.* **9**, 38–41 (2016).
41. D. Kong *et al.*, Xiaolangdi Dam: A valve for streamflow extremes on the lower Yellow River. *J. Hydrol.* **606**, 127426 (2022).
42. X. Zhu, H. Pang, "Xiaolangdi reservoir's role in water andsediment regulation" in *Encyclopedia of Lakes and Reservoirs, Encyclopedia of Earth Sciences Series*, (Springer, 2012), pp. 925–927.
43. Z. X. Cao, J. Li, G. Pender, Q. Q. Liu, Whole-process modeling of reservoir turbidity currents by a double layer-averaged model. *J. Hydraul. Eng.* **141**, 04014069 (2015).
44. P. Hu, Z. X. Cao, G. Pender, G. M. Tan, Numerical modelling of turbidity currents in the Xiaolangdi Reservoir, Yellow River, China. *J. Hydrol.* **464**, 41–53 (2012).
45. T. Y. Wei *et al.*, Three-dimensional gravity-current flow within a subaqueous bend: Spatial evolution and force balance variations. *Sedimentology* **60**, 1668–1680 (2013).
46. Z. Y. Wang, C. H. Hu, Strategies for managing reservoir sedimentation. *Int. J. Sediment Res.* **24**, 369–384 (2009).
47. G. Wang, B. Wu, Z. Wang, Sedimentation problems and management strategies of Sanmenxia Reservoir, Yellow River, China. *Water Resour. Res.* **41**, 2004WR003919 (2005).
48. C. Pirmez, J. Imran, Reconstruction of turbidity currents in Amazon Channel. *Mar. Pet. Geol.* **20**, 823–849 (2003).
49. I. Jegou, B. Savoye, C. Pirmez, L. Droz, Channel-mouth lobe complex of the recent Amazon Fan: The missing piece. *Mar. Geol.* **252**, 62–77 (2008).
50. T. Schwenk, V. Spieß, C. Hübscher, M. Breitzke, Frequent channel avulsions within the active channel–levee system of the middle Bengal Fan–an exceptional channel–levee development derived from Parasound and Hydrosweep data. *Deep Sea Res. Part II: Top. Stud. Oceanogr.* **50**, 1023–1045 (2003).
51. O. Andrieux, C. K. Cooper, J. Wood, *Turbidity Current Measurements in the Congo Canyon* (Offshore Technology Conference, 2013).
52. S. Thorez, U. Lemmin, D. A. Barry, K. Blanckaert, Hydro-sedimentary processes of a plunging hyperpycnal river plume revealed by synchronized remote imagery and gridded current measurements. *Water Resour. Res.* **60**, e2023WR035907 (2024).
53. H. Ma *et al.*, Two-layer formulation for long-runout turbidity currents: Theory and bypass flow case. *J. Fluid Mech.* **1009**, A19 (2025).
54. S. C. Ruffell *et al.*, Time-lapse surveys reveal patterns and processes of erosion by exceptionally powerful turbidity currents that flush submarine canyons: A case study of the Congo Canyon. *Geomorphology* **463**, 109350 (2024).
55. M. S. Heijnen *et al.*, Rapidly-migrating and internally-generated knickpoints can control submarine channel evolution. *Nat. Commun.* **11**, 3129 (2020).
56. S. C. R. Dennis, F. T. Smith, Steady flow through a channel with a symmetrical constriction in the form of a step. *Proc. R. Soc. Lond. A Math. Phys. Sci.* **372**, 393–414 (1980).
57. F. Durst, W. F. Schierholz, A. M. Wunderlich, Experimental and numerical investigations of plane duct flows with sudden contraction. *J. Fluids Eng.* **109**, 376–383 (1987).
58. P. Hu, T. Pähtz, Z. He, Is it appropriate to model turbidity currents with the three-equation model? *J. Geophys. Res.: Earth Surf.* **120**, 1153–1170 (2015).
59. M. B. Pittaluga, A. Frascati, O. Falivene, A gradually varied approach to model turbidity currents in submarine channels. *J. Geophys. Res. Earth Surf.* **123**, 80–96 (2018).
60. T. H. Ellison, J. S. Turner, Turbulent entrainment in stratified flows. *J. Fluid Mech.* **6**, 423–448 (1959).
61. H. B. Ma *et al.*, The exceptional sediment load of fine-grained dispersal systems: Example of the Yellow River, China. *Sci. Adv.* **3**, e1603114 (2017).
62. H. Ma *et al.*, Universal relation with regime transition for sediment transport in fine-grained rivers. *Proc. Natl. Acad. Sci. U.S.A.* **117**, 171–176 (2020).
63. A. J. Moodie *et al.*, Suspended-sediment induced stratification inferred from concentration and velocity profile measurements in the lower Yellow River, China. *Water Resour. Res.* **58**, e2020WR027192 (2020).
64. G. Parker, M. Garcia, Y. Fukushima, W. Yu, Experiments on turbidity currents over an erodible bed. *J. Hydraul. Res.* **25**, 123–147 (1987).

Downloaded from https://www.pnas.org by UNIVERSITY OF ILLINOIS URBANA CHAMPAIGN; BIOLOGY LIB E on May 26, 2026 from IP address 130.126.255.117.